

clDice - a Topology-Preserving Loss Function for Tubular Structure Segmentation

Suprosanna Shit ^{*1}, Johannes C. Paetzold ^{*1}, Anjany Sekuboyina¹, Andrey Zhylka², Ivan Ezhov¹, Alexander Unger¹, Josien P. W. Pluim², Giles Tetteh¹, and Bjoern H. Menze¹

¹ Department of Informatics, Technical University of Munich

² Department of Biomedical Engineering, Eindhoven University of Technology
johannes.paetzold@tum.de, suprosanna.shit@tum.de

Abstract. Accurate segmentation of tubular, network-like structures, such as vessels, neurons, or roads, is relevant to many fields of research. For such structures, the topology is their most important characteristic, e.g. preserving connectedness: in case of vascular networks, missing a connected vessel entirely alters the blood-flow dynamics. We introduce a novel similarity measure termed *clDice*, which is calculated on the intersection of the segmentation masks and their (morphological) skeletons. Crucially, we theoretically prove that *clDice* guarantees topological correctness for binary 2D and 3D segmentation. Extending this, we propose a computationally efficient, differentiable *soft-clDice* as a loss function for training arbitrary neural segmentation networks. We benchmark the *soft-clDice* loss for segmentation on four public datasets (2D and 3D). Training on *soft-clDice* leads to segmentation with more accurate connectivity information, higher graph similarity, and better volumetric scores.

Keywords: Topology, Skeleton, Segmentation, Loss Function

1 Introduction

Segmentation of *tubular* and *curvilinear* structures is an essential problem in numerous domains, such as clinical and biological applications (blood vessel and neuron segmentation from microscopic, optoacoustic, and radiology images), remote sensing applications (road network segmentation from satellite images), industrial quality control, etc. In these domains, a topologically accurate segmentation is necessary to guarantee error-free down-stream tasks, e.g. computational hemodynamics, Alzheimer’s disease prediction [10], or stroke modeling [11]. Analogous to most other image segmentation tasks, the two most commonly used categories of quantitative performance measures for evaluating segmentation accuracy of *tubular* structures, are 1) overlap based measures such as dice-score, precision, recall, and Jaccard index; and 2) volumetric distance measures such as the Hausdorff distance and the Mahalanobis distance [12,28,24,8].

^{*} The authors contributed equally to the work

However in most segmentation problems, where the object of interest is 1) locally a *tubular* structure and 2) globally forms a *network*, the most important characteristic to be preserved for the success of the subsequent tasks is the connectivity of the global network topology. Note that *network* in this context implies a physically connected structure, such as a vessel network, a road network, etc., which is also the primary structure of interest that is to be extracted as accurately as possible from the given image data. As an example, one can refer to brain vasculature analysis, where a missed vessel segment in the segmentation mask can pathologically be interpreted as a stroke or may lead to dramatic changes in a global simulation of blood flow. On the other hand, limited over- or under-segmentation can be tolerated, because a marginally thicker or thinner segmentation of a vessel does not affect clinical diagnosis.

For evaluating segmentation in such tubular-network structures, traditional performance indices are sub-optimal. For example, dice and Jaccard rely on the average voxel-wise hit or miss prediction [33]. In a task like network-topology extraction, a spatially contiguous sequence of correct voxel prediction is more meaningful than a spurious correct prediction. Further, a globally averaged metric does not equally weight tubular-structures with large, medium and small radii (cf. Fig 1). In real vessel datasets, where vessels of wide radius ranges exist, e.g. 30 μm for arterioles [35,4] and 5 μm for capillaries, training on a globally averaged loss induces a strong bias towards the volumetric segmentation of large vessels. This is pronounced in imaging modalities, such as fluorescence microscopy [35,42] and optoacoustic, which focus on mapping small capillary structures. In Figure 1, an example illustrates the sub-optimality of traditional scores in some scenarios.

Furthermore, most traditional metrics are ambiguous when some of the objects of interest are of the same order as the resolution of the signal. Single-voxel shifts in the prediction can change the topology of the network while maintaining a similar global segmentation score, thus making the metric difficult to interpret

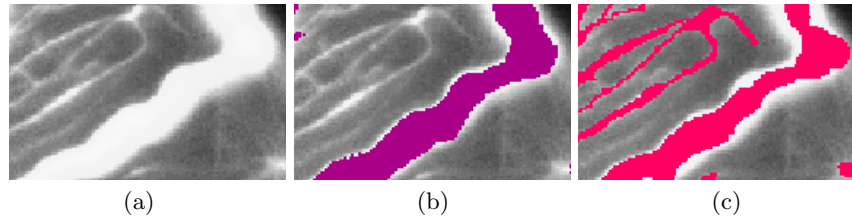


Fig. 1. Motivation: (a) Shows an exemplary 2D slice of real microscopic data, (b) and (c) are two random segmentation results which achieve similar scores that are of identical quality in terms of the traditional dice score (not from our presented model). Note that (b) does not capture any of the small vessels while segmenting the large vessel very accurately; on the other side segmentation (c) captures all vessels in the image while being less accurate on the diameter of the large vessel. From a topology or network perspective, segmentation (c) is preferred.

[33]. To this end, we are interested in a topology-aware segmentation of an image, eventually enabling correct network extraction. Therefore, we ask the following research questions:

- Q1. What is a good measure to benchmark segmentation algorithms for tubular, linear and curvilinear structure segmentation while guaranteeing the preservation of the network-topology?
- Q2. Can we use this *improved measure* as a loss function for neural networks?

1.1 Related Literature

Achieving topology preservation can be crucial to obtain meaningful segmentation, particularly for elongated and connected shapes, e.g. vascular structures or roads. However analyzing preservation of topology while simplifying geometries is a difficult analytical and computational problem [5,6].

For binary geometries, various algorithms based on thinning and medial surfaces have been proven to be topology-preserving according to varying definitions of topology [13,15,16,23]. For non-binary geometries, existing methods applied topology and connectivity constraints onto variational and Markov random field-based segmentation methods: tree shape priors for vessel segmentation [31], graph representation priors to natural images [1], higher-order cliques which connect superpixels to road network extraction [39], or integer programming to general curvilinear structures [36], among others [7,21,20,22,25,29,38,41]. Furthermore, topological priors of containment and detachment were applied to convolutional neural network (CNN) based segmentation of image features in histology scans [2].

It is critical to differentiate between enforcing a topology prior and training using a topology-preserving loss function. Minimizing a topology-preserving loss function guarantees a perfect topology of a segmentation mask. Recently, some approaches have directly implemented topology-aware loss functions for structure segmentation in CNNs. Hu et al. proposed a continuous-valued loss function based on the Betti number [9]. Mosinska et al. claimed that pixel-wise loss-functions are unsuitable for topology and used selected filter responses from a VGG19 network as an additional penalty [19]. Nonetheless, the latter approach does not prove topology preservation. The method by Hu et al. is based on a matching of critical points, which, according to the authors makes the computation very expensive and error-prone for real image-sized patches [9]. Furthermore, these approaches have not been extended to three dimensional (3D) data.

1.2 Our Contributions

The objective of this paper is topology preservation while segmenting tubular objects. We introduce a novel connectivity-aware similarity measure named *clDice* for bench-marking tubular-segmentation algorithms. Importantly, we provide theoretical guarantees for the topological correctness of the *clDice* for binary 2D

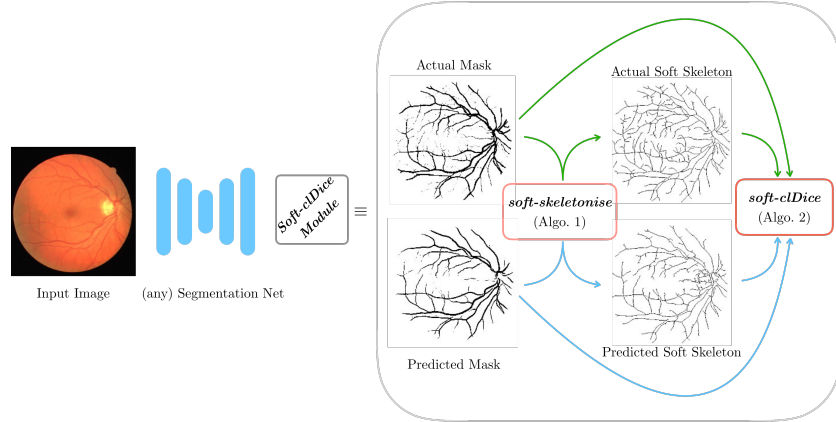


Fig. 2. Schematic overview of our proposed method: Our proposed *clDice* loss can be applied to any arbitrary segmentation network. The soft-skeletonization can be easily implemented using pooling functions from any standard deep-learning toolbox.

and 3D segmentation. As a consequence of its formulation based on morphological skeletons, our measure pronounces the network’s topology instead of equally weighting every voxel. Using a differentiable soft-skeletonization, we show that the *clDice* measure can be used to train neural networks.

We show experimental results for various 2D and 3D network segmentation settings and tasks to demonstrate the practical applicability of our proposed similarity measure and loss function.

2 Let’s Emphasize *Connectivity*

In this section we first introduce the *clDice* as a similarity measure and subsequently introduce a differentiable loss function namely *soft-clDice*.

***clDice* Measure:** We propose a novel connectivity-preserving metric to evaluate tubular and linear structure segmentation based on intersecting skeletons with masks. We call this metric a centerline-in-mask-dice-coefficient or *clDice*. We consider two binary masks: the ground truth mask (V_L) and the predicted segmentation masks (V_P). First, the skeletons S_P and S_L are extracted from V_P and V_L respectively. Subsequently, we compute the fraction of S_P that lies within V_L , which we call *Topology Precision* or $Tprec(S_P, V_L)$, and vice-a-versa we obtain *Topology Sensitivity* or $Tsens(S_L, V_P)$ as defined below;

$$Tprec(S_P, V_L) = \frac{|S_P \cap V_L|}{|S_P|}; \quad Tsens(S_L, V_P) = \frac{|S_L \cap V_P|}{|S_L|} \quad (1)$$

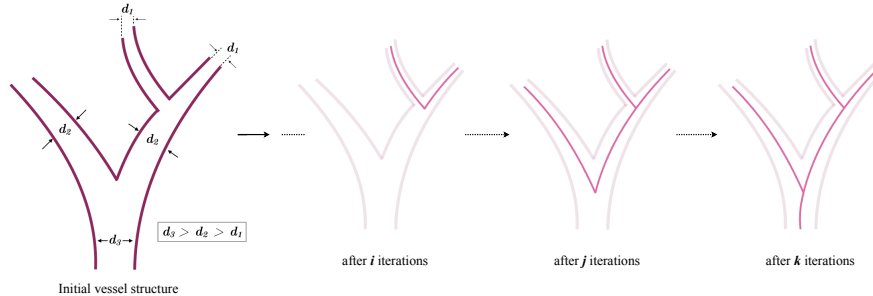


Fig. 3. Based on the initial vessel structure (purple), sequential bagging of skeleton voxels (red) via iterative skeletonization leads to a complete skeletonization, where d denotes the diameter and $k > j > i$ iterations.

We observe that the measure $Tprec(S_P, V_L)$ is susceptible to false positives in the prediction while the measure $Tsens(S_L, V_P)$ is susceptible to false negatives. This explains our rationale behind referring to the $Tprec(S_P, V_L)$ as topology's precision and to the $Tsens(S_L, V_P)$ as its sensitivity. Since we want to maximize both precision and sensitivity (recall), we construct the *clDice* to be symmetric with respect to both the measures:

$$clDice(V_P, V_L) = 2 \times \frac{Tprec(S_P, V_L) \times Tsens(S_L, V_P)}{Tprec(S_P, V_L) + Tsens(S_L, V_P)} \quad (2)$$

Soft-clDice as a Loss Function using Soft-skeletonization: Different approaches to extract skeletons have been described, very popular are approaches using the Euclidean distance transform or approaches which utilize repeated morphological thinning. Although Euclidean distance transform has been used on multiple occasions to induce skeletons [30,40], it is a discrete operation and, to the best of our knowledge, an end-to-end differentiable approximation remains to be developed. This prevents the usage of Euclidean distance transform as a loss function for training neural networks. On the contrary, morphological thinning is a sequence of dilation and erosion operations [c.f. Fig. 2]. Min- and max filters are commonly used as the grey-scale alternative of morphological dilation and erosion. Motivated by this, we propose 'soft-skeletonization', where an iterative min- and max-pooling is applied as a proxy for morphological erosion and dilation. The Algorithm 1 describes the iterative processes involved in its computation. The hyper-parameter k involved in its computation represents the iterations and has to be greater than or equal to the maximum radius for the tube-like structure. In our experiments, this parameter depends on the dataset. E.g. $k = 5-10$ for the synthetic and real 3D vessel data. Choosing a larger k does not reduce performance but increases computation time. On the other hand, a too low k leads to incomplete skeletonization. In Figure 1, the successive steps of our skeletonization are intuitively represented. In the early iterations, the structures with a small radius are skeletonized and preserved until the later iterations

Fig. 4. Algorithm Description: In Algorithm 1, I is the mask to be *soft-skeletonized* and k the number of iterations for skeletonization. In Algorithm 2, V_P is a real-valued probabilistic prediction from a segmentation network and V_L is the true mask. We denote Hadamard product using \circ .

Algorithm 1: soft-skeleton	Algorithm 2: soft-clDice
Input: I, k $I' \leftarrow \text{maxpool}(\text{minpool}(I))$ $S \leftarrow \text{ReLU}(I - I')$ for $i \leftarrow 0$ to k do $I \leftarrow \text{minpool}(I)$ $I' \leftarrow \text{maxpool}(\text{minpool}(I))$ $S \leftarrow S + (1 - S) \circ \text{ReLU}(I - I')$ end Output: S	Input: V_P, V_L $S_P \leftarrow \text{soft-skeleton}(V_P)$ $S_L \leftarrow \text{soft-skeleton}(V_L)$ $Tprec(S_P, V_L) \leftarrow \frac{ S_P \circ V_L + \epsilon}{ S_P + \epsilon}$ $Tsens(S_L, V_P) \leftarrow \frac{ S_L \circ V_P + \epsilon}{ S_L + \epsilon}$ $clDice \leftarrow 2 \times \frac{Tprec(S_P, V_L) \times Tsens(S_L, V_P)}{Tprec(S_P, V_L) + Tsens(S_L, V_P)}$ Output: $clDice$

when the thicker structures also become skeletonized. This enables the extraction of a parameter-free, morphologically motivated soft-skeleton on real-valued data. The aforementioned soft-skeletonization enables us to use *clDice* as a fully differentiable, real-valued, optimizable measure. The Algorithm 2 describes its implementation. We refer to this as the *soft-clDice*.

3 Topology Preserving Guarantees for clDice

Betti numbers describe and quantify topological differences in algebraic topology. The first three betti numbers (b_0 , b_1 , and b_2) comprehensively capture the manifolds appearing in 2D and 3D topological space. Specifically,

- b_0 represents the number of distinct *connected-components*,
- b_1 represents the number of *circular holes* [c.f. Fig. 5], and
- b_2 represents the number of *cavities* [c.f. Fig. 5] (Only applicable in 3D)



Fig. 5. Examples of the topology terminology. Left, a hole in 2D, in the middle a hole in 3D and right a cavity inside a sphere in 3D.

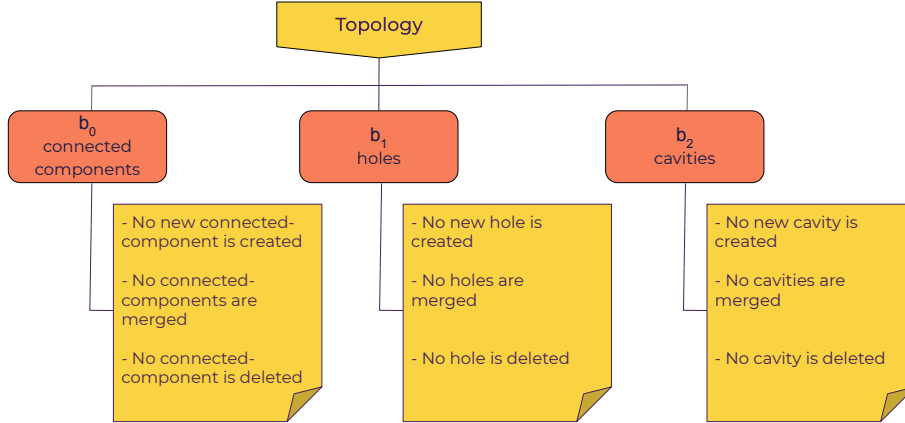


Fig. 6. Taxonomy of the *iff* conditions to preserve topology in 3D [13,14].

Based on the above notation we formulate the conditions of topology preservation between a labeled binary mask (V_L) and a predicted binary mask (V_P) according to Kong et al. [13] in 3D in Fig 6.

Topology-preserving skeletonization: Thinning using morphological operations (skeletonization) is topology-preserving [23]. Therefore, all the topological differences between the labeled mask and a predicted mask are preserved in the topological differences between the skeletons of an actual mask and a predicted mask, respectively. Note that this holds for the skeletons of both the foreground and background regions. Following this, we postulate that topology preservation of a binary mask through its skeletons using two voxel-specific conditions:

Top 1 - No ghosts in skeleton: $S_P \subset V_L$; the predicted skeleton is completely included in the true mask. Otherwise, if $S_P \not\subset V_L$ implies ghosts in V_P .

Top 2 - No misses in skeleton: $S_L \subset V_P$; the true skeleton is completely included in the predicted mask. Otherwise, if $S_L \not\subset V_P$ implies misses in V_P .

Table 1 redefines the topology-preserving conditions defined for masks (cf. Fig. 6) in terms of Top 1 and Top 2 properties described above. Essentially, it summarizes the necessary conditions when the topology is not preserved based on these two key properties, in terms of the foreground and background skeleton.

Denoting the set of foreground and background voxels with subscripts f and b , respectively, we represent the voxels in the true mask with L_f and L_b ($= 1 - L_f$) and the voxel in the predicted mask with P_f and P_b ($= 1 - P_f$). We define loss functions for the foreground and background classes as:

Table 1. Necessary violation of skeleton properties (Top 1 and Top 2) for each of the topological changes.

Topological Changes		foreground	background
I.	New connected-component is created	Top 1	-
II.	Connected-components are merged	-	Top 2
III.	Connected-component is deleted	Top 2	-
IV.	New hole is created	-	Top 1
V.	Holes have been merged	Top 2	-
VI.	Hole is deleted	-	Top 2
VII.	New cavity is created	-	Top 1
VIII.	Cavities are merged	Top 2	-
IX.	Cavity is deleted	-	Top 2

$$\text{Topology loss for foreground: } \text{clDice}_f = \text{clDice}(P_f, L_f) \quad (3)$$

$$\text{Topology loss for background: } \text{clDice}_b = \text{clDice}(P_b, L_b) \quad (4)$$

Equipped with this notation and with the conditions in Table 1, we prove the following aspects of clDice :

1. Optimal clDice score in voxel-specific conditions achieves perfect topology.
2. Minimizing topology mismatch implies maximizing clDice .
3. Any misses or ghosts in the skeleton of the prediction decrease the clDice .

Theorem 1. *If the $\text{clDice}_f = \text{clDice}_b = 1$, topology is preserved.*

Proof. $\text{clDice} = 1 \implies T_{\text{prec}} = 1$ and $T_{\text{sens}} = 1$. By definition of topology precision and sensitivity in Equation 1, we know that: $T_{\text{prec}} = 1 \implies S_P \subset V_L$ and $T_{\text{sens}} = 1 \implies S_L \subset V_P$. Which means all sufficient conditions to preserve topology, i.e. **Top 1** and **Top 2**, are satisfied and hence topology is preserved. \square

We formulate the following theorems to show that minimizing topology mismatch implies maximizing clDice .

Theorem 2. *Any ghosts in the skeleton of the prediction decrease the clDice .*

Proof. Let us consider a true skeleton $S_L = \{h_i\}_{i=1}^{N_L}$ of a true mask V_L and a perfectly predicted skeleton $S_{P,\text{opt}} = \{g_i\}_{i=1}^{N_{\text{opt}}}$ without any ghosts and misses from a predicted mask $V_{P,\text{opt}}$, where g_i and h_i are the skeleton points of $S_{P,\text{opt}}$ and S_L respectively. Since there is no ghost or missing components in the skeleton, we have $S_{P,\text{opt}} \subset V_L$ and $S_L \subset V_{P,\text{opt}}$. Which implies that skeletons S_L and $S_{P,\text{opt}}$ as well as corresponding mask V_L and $V_{P,\text{opt}}$ have the same topology. Considering the topological precision ($T_{\text{prec},\text{opt}}$) for $S_{P,\text{opt}}$:

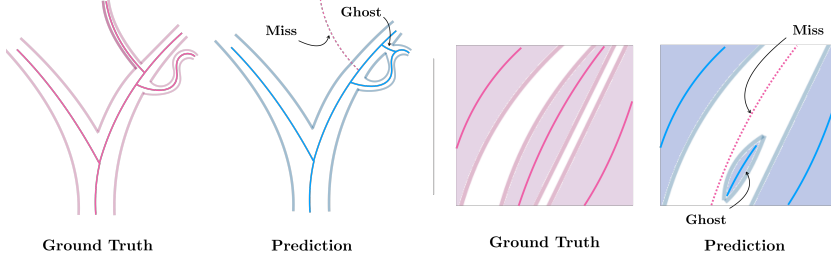


Fig. 7. Intuitive depictions of ghosts and misses in the prediction, for the skeleton of the foreground (left) and the skeleton of the background (right).

$$\begin{aligned}
 Tprec_{opt} &= \sum_{i=1}^{N_{opt}} \frac{g_i V_L(g_i)}{\sum_{j=1}^{N_{opt}} g_j} ; \quad [\text{since } V_L(g_i) = 1 \quad \forall i = \overline{1, N_{opt}}] \\
 &= \sum_{i=1}^{N_{opt}} \frac{g_i}{\sum_{j=1}^{N_{opt}} g_j} = 1.
 \end{aligned} \tag{5}$$

Now, without loss of generality, let us consider the case of a topological change, such that for a predicted mask $V_{P,F}$ with no misses in the skeleton, a ghost skeleton $S_{P,F} = \{f_i\}_{i=1}^M$ was reconstructed that contains connected segments outside V_L . Let's denote $clDice$ in the perfect prediction and prediction with ghost as $clDice_{opt}$ and $clDice_F$ respectively.

$$\text{Ghost Skeleton: } \exists j \in \overline{1, M} \text{ such that } V_L(f_j) = 0. \tag{6}$$

Considering the topological precision ($Tprec_F$) for $S_{P,F}$:

$$\begin{aligned}
 Tprec_F &= \sum_{i=1}^M \frac{f_i V_L(f_i)}{\sum_{j=1}^M f_j} < \sum_{i=1}^M \frac{f_i}{\sum_{j=1}^M f_j} = 1 \\
 Tprec_F &< Tprec_{opt}.
 \end{aligned} \tag{7}$$

Since the skeletonization algorithm preserves topology and there is no missing components in the prediction $V_{P,F}$, $S_L \subset V_{P,F}$. Considering the topological sensitivities $Tsens_F$ and $Tsens_{opt}$ of $V_{P,F}$ and $V_{P,opt}$ respectively,

$$Tsens_F = \sum_{i=1}^{N_L} \frac{h_i V_{P,F}(h_i)}{\sum_{j=1}^{N_L} h_j} = 1 = \sum_{i=1}^{N_L} \frac{h_i V_{P,opt}(h_i)}{\sum_{j=1}^{N_L} h_j} = Tsens_{opt}. \tag{8}$$

Combining (7) and (8) in the $clDice$ (2) and given that values of sensitivity and precision belong to $[0, 1]$ by definition, we obtain the following:

$$\begin{aligned} \text{clDice}_F &= 2 \frac{\text{Tsens}_F \times \text{Tprec}_F}{\text{Tsens}_F + \text{Tprec}_F} < 2 \frac{\text{Tsens}_{opt} \times \text{Tprec}_{opt}}{\text{Tsens}_{opt} + \text{Tprec}_{opt}} = \text{clDice}_{opt} = 1 \\ \text{clDice}_F &< \text{clDice}_{opt}. \end{aligned} \quad (9)$$

□

Theorem 3. Any misses in the skeleton of the prediction decrease the clDice.

Proof. Similar to the proof of Theorem 1 we consider a true mask V_L and a predicted mask $V_{P,opt}$, with their respective true skeleton $S_L = \{h_i\}_{i=1}^{N_L}$ and a perfectly predicted skeleton $S_{P,opt} = \{g_i\}_{i=1}^{N_{opt}}$ without any ghosts and misses. Since there are no ghost or missing components in the skeleton, we have $S_{P,opt} \subset V_L$ and $S_L \subset V_{P,opt}$; considering the topological sensitivity (Tsens_{opt}) for $S_{P,opt}$:

$$\text{Tsens}_{opt} = \sum_{i=1}^{N_L} \frac{h_i V_{P,opt}(h_i)}{\sum_{j=1}^{N_L} h_j} = 1. \quad (10)$$

Similar to the formulation of the Theorem 1, without the loss of generality, let us consider the case of a topological change, for a predicted mask $V_{P,F}$ with no ghosts, but with one or more misses in the skeleton $S_{P,F} = \{f_i\}_{i=1}^M$ such that there exist a connected segment in the true skeleton which is outside of $V_{P,F}$. Let's denote clDice in the optimal (perfect) prediction and prediction with misses as clDice_{opt} and clDice_F respectively.

$$\text{Missing Skeleton: } \exists j \in \overline{1, N_L} \quad V_{P,F}(h_j) = 0. \quad (11)$$

Considering the topological sensitivity (Tsens_F) for $S_{P,F}$:

$$\begin{aligned} \text{Tsens}_F &= \sum_{i=1}^{N_L} \frac{h_i V_{P,F}(h_i)}{\sum_{j=1}^{N_L} h_j} < \sum_{i=1}^{N_L} \frac{h_i}{\sum_{j=1}^{N_L} h_j} = 1. \\ \text{Tsens}_F &< \text{Tsens}_{opt}. \end{aligned} \quad (12)$$

Since the skeletonization algorithm preserves topology and there are no ghosts in the predicted skeleton $S_{P,F}$, $S_{P,F} \subset V_L$. Considering the topological precisions: Tprec_F and Tprec_{opt} of $V_{P,F}$ and $V_{P,opt}$ respectively,

$$\text{Tprec}_F = \sum_{i=1}^M \frac{f_i V_L(f_i)}{\sum_{j=1}^M f_j} = 1 \stackrel{(5)}{=} \text{Tprec}_{opt}. \quad (13)$$

In analogy to Theorem 1, based on (12) and (13) we conclude that,

$$\text{clDice}_F < \text{clDice}_{opt}. \quad (14)$$

□

4 Experiments

Since our objective here is to preserve topology while achieving accurate segmentations, we combine our proposed *soft-clDice* with *soft-Dice* as following:

$$\mathcal{L}_c = \alpha(1 - \text{soft-Dice}) + (1 - \alpha)(1 - \text{soft-clDice}) , \alpha \in [0, 0.5] \quad (15)$$

In stark contrast to previous works, where segmentation and centerline prediction has been learned jointly as multi-task learning [37,34], we are not interested in learning the centerline. We are interested in learning a topology-preserving segmentation. Therefore, we restrict our experimental choice of alpha to $\alpha \in [0, 0.5]$.

We use the proposed *clDice* to evaluate the segmentation performance of two state-of-the-art network architectures: i) a 2D and 3D U-Net[26,3], and ii) a 2D and 3D fully connected networks (FCN) [34]. As baselines, we use the same architectures trained using generalized *soft-Dice* [17,32].

4.1 Datasets

In all, we employ four datasets for validating *clDice* and *soft-clDice* as a measure and an objective function, respectively. In 2D, we test the DRIVE retina dataset ³ and the Massachusetts Roads dataset [18] ⁴. In 3D, a synthetic and a real brain vessel dataset. The generation of the synthetic vessel data is described in [27], additionally, we add a Gaussian noise term to this generated data ⁵. The real 3D dataset consists of multi-channel volumetric scans of the brain vasculature (voxel size: $(3\mu\text{m}^3)$), which were obtained using light-sheet microscopy of tissue cleared Murine brains, and made publicly available in [35] ⁶.

For the DRIVE vessel segmentation dataset, we perform three-fold cross-validation with 30 images and deploy the best performing model on the test set with 10 images. For the Massachusetts Roads dataset, we choose a subset of 120 images (ignoring imaged without a network of roads) for three-fold cross-validation and test the models on the 13 official test images. For the 3D synthetic dataset, we perform experiments using 15 single-channel volumes for training, 2 for validation, and 5 for testing. For the real 3D dataset, we use 11 volumes for training, 2 for validation and 4 for testing. In each of these cases, we report the performance of the model with the highest dice score on the validation set.

4.2 *clDice* in Practice.

As described in Section 3, in theory, *clDice* holds and explains a two-class case and should be computed on both the foreground and the background channels.

³ <https://drive.grand-challenge.org/>

⁴ <https://www.cs.toronto.edu/~vmnih/data/>

⁵ <https://github.com/gieseckow/deepvesselnet/wiki/Datasets>

⁶ <http://discotechnologies.org/VesSAP/>

However, in practice, this is hindered by an imbalance in the foreground and background classes (e.g. in vessel and road datasets).

The class imbalance would substantially enhance the computational complexity in calculating the skeletons on the majority class (typically the background class). Thus, we calculate the *clDice* only on the foreground. Note that this is not detrimental to the performance of *clDice* in the context of the datasets considered in our experiments. We attribute this to the non-applicability of the necessary conditions specific to the background (i.e. II, IV, VI, VII, and IX in Table 1), as explained below:

- II. → In tubular structures, all foreground objects are eccentric (or anisotropic). Therefore isotropic skeletonization will highly likely produce a ghost in the foreground.
- IV. → Creating a hole outside the labeled mask means adding a ghost in the foreground. Creating a hole inside the labeled mask is extremely unlikely because no such holes exist in our training data.
- VI. → The deletion of a hole without creating a miss is extremely unlikely because of the sparsity of the data.
- VII. (only for 3D) → Creating a cavity is very unlikely because no cavities exist in our training data.
- IX. (only for 3D) → Cavities do not exist in the real dataset.

4.3 Evaluation Metrics

We compare the performance of various experimental setups using two types metrics: overlap-based and topology-based.

1. Overlap-based: Dice coefficient, Accuracy, and the proposed *clDice*.
2. Topology-based: We extract a vascular graph from the skeleton of the predicted segmentation and compute relative accuracy ($1 - \text{relative error}$) of total vascular network length (Dist.), and the ratio of detected bifurcation points (Bifurc.) with respect to the ground truth, which describes graph similarity. Finally, we measure topological similarity using the Euler characteristic, $\chi = V - E + F$, where V is the number of vertices, E is the number of edges and F is the number of faces. We report the relative Euler characteristic error (χ_{ratio}), as the ratio of the χ of the predicted mask and that of the ground truth. Note that a χ_{ratio} closer to one is preferred.

4.4 Discussion

We trained a U-Net and an FCN for the different loss functions in identical settings. In Table 2 we present an experiment, where we trained five models with a varying α from (0.1 to 0.5) on the DRIVE dataset. We observe that including *soft-clDice* in any proportion leads to improved topological similarity. Further, increasing the α consistently improves the *clDice* measure. The inclusion of *soft-clDice* improves dice and accuracy, and more importantly preserves

Table 2. Experimental results for 2D networks on the DRIVE dataset and the Massachusetts road dataset. Bold numbers indicate the best performance. All images are RGB (3 ch). Compared to *soft-Dice*, we observe that *soft-clDice* results in improved traditional scores, *clDice* as well as Euler characteristic χ_{ratio} , for varying values of α .

Data	Network	Loss	Dice	clDice	Acc.	Dist.	Bifurc.	χ_{ratio}
DRIVE retina	FCN	<i>soft-dice</i>	78.23	78.02	96.27	0.82	0.72	1.35
		$\mathcal{L}_c, \alpha = 0.1$	78.36	79.02	96.25	0.83	0.78	1.32
		$\mathcal{L}_c, \alpha = 0.2$	78.75	80.22	96.29	0.83	0.79	1.10
		$\mathcal{L}_c, \alpha = 0.3$	78.29	80.28	96.20	0.81	0.73	1.08
		$\mathcal{L}_c, \alpha = 0.4$	78.00	80.43	96.11	0.81	0.77	1.17
		$\mathcal{L}_c, \alpha = 0.5$	77.76	80.95	96.04	0.83	0.79	0.97
DRIVE retina	U-Net	<i>soft-dice</i>	74.25	75.71	95.63	0.73	0.58	1.56
		$\mathcal{L}_c, \alpha = 0.5$	75.21	76.86	95.82	0.77	0.72	1.08
Road-Network	U-Net	<i>soft-dice</i>	70.98	81.45	96.38	0.86	0.73	2.09
		$\mathcal{L}_c, \alpha = 0.5$	71.16	82.12	96.30	0.88	0.74	1.48

Table 3. Experimental results for 3D U-Nets and 3D FCNs on synthetic and real data. We observe a consistent performance improvement for real data with the combination of *soft-clDice* and *soft-dice*. Bold numbers indicate the best performing loss functions on the same network with the identical train, validation and test set. Overall *clDice* leads to results that are preferable to those obtained with soft-Dice

Data	Network	Loss	Dice	clDice	Acc.	Dist.	Bifurc.	χ_{ratio}
Synthetic	FCN, 1 ch	<i>soft-dice</i>	99.41	99.45	99.97	0.92	0.91	0.81
		$\mathcal{L}_c, \alpha = 0.5$	99.16	99.77	99.96	0.92	0.91	0.82
	U-Net, 1 ch	<i>soft-dice</i>	99.61	99.90	99.98	0.88	0.86	0.83
		$\mathcal{L}_c, \alpha = 0.5$	98.73	99.90	99.94	0.88	0.86	0.84
Vessap data	FCN, 1 ch	<i>soft-dice</i>	75.28	90.98	89.88	0.87	0.72	1.51
		$\mathcal{L}_c, \alpha = 0.5$	85.57	96.16	95.09	0.82	0.88	0.97
	FCN, 2 ch	<i>soft-dice</i>	78.54	92.03	91.66	0.90	0.82	1.33
		$\mathcal{L}_c, \alpha = 0.5$	85.28	95.75	94.91	0.91	0.91	1.11
	U-Net, 1 ch	<i>soft-dice</i>	87.11	95.03	95.78	0.92	0.82	0.77
		$\mathcal{L}_c, \alpha = 0.5$	86.94	95.28	95.86	0.94	0.83	0.78
	U-Net, 2 ch	<i>soft-dice</i>	80.20	93.05	92.33	0.95	0.93	1.24
		$\mathcal{L}_c, \alpha = 0.5$	83.96	96.10	94.18	0.96	0.89	0.92

connectedness, improves the topological and graph similarity. In the case of 3D data, we observe similar trends, however it is not so pronounced in the synthetic data. We attribute this to the relatively simple features of the synthetic data, which has a high signal-to-noise ratio and lacks significant illumination variation. However, we observe significant improvements for all measures in case of the more complex multi-channel microscopic vessel data, see Figure 8. Despite not optimizing the *soft-clDice* on the background class, all of our networks converge to superior segmentation results. This not only reinforces our assumptions on

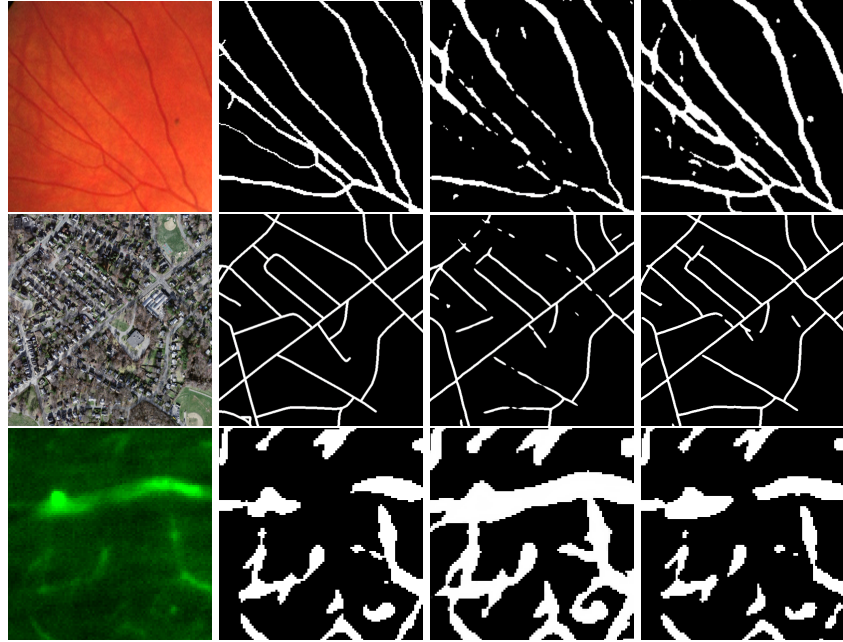


Fig. 8. Qualitative results: from top to bottom, for the DRIVE retina, the Massachusetts road dataset and for 2D slices from our real 3D vessel dataset. From left to right, the real image, the label, the prediction using soft-dice and the U-Net predictions using $\mathcal{L}_c(\alpha = 0.5)$, respectively. This indicates that $clDice$ segments road connections and retina vessel connections which the soft-dice loss misses, but also does not segment false-positive vessels in 3D.

dataset-specific necessary conditions but validates the practical applicability of our loss. Our findings hold for the different network architectures, for 2D or 3D, and for tubular or curvilinear structures, strongly indicating its generalizability to analogous binary segmentation tasks.

In Figure 8, typical results for our datasets are depicted. Our networks trained on the proposed loss term recovers connections which were false negatives when trained with the soft-dice loss. Interestingly, in the real 3D vessel dataset, the soft-dice loss over segments stray light from large vessels, while the proposed loss function does not because of its topology-preserving nature.

5 Conclusions

We introduce $clDice$, a novel connectivity-preserving similarity measure for tubular structure segmentation. Importantly, we present a theoretical guarantee that $clDice$ enforces topology preservation in 3D. First, we use the new metric to benchmark segmentation quality from a topology-preserving perspective. Next,

we use a differentiable version, *soft-clDice*, in a loss function, to train state-of-the-art 2D and 3D neural networks. We find that training on *soft-clDice* leads to segmentations with more accurate connectivity information, better Euler characteristics and improved Dice and Accuracy. Our *soft-clDice* is computationally efficient and can be readily deployed in other tubular or linear-structured object segmentation tasks such as neuron segmentation in biomedical imaging, crack detection in industrial quality control or remote sensing.

Acknowledgement

Suprosanna Shit, Andrey Zhylka and Ivan Ezhov are supported by the Translational Brain Imaging Training Network(TRABIT) under the European Union's 'Horizon 2020' research & innovation program (Grant agreement ID: 765148). With the support of the Technical University of Munich Institute for Advanced Study, funded by the German Excellence Initiative. Johannes C. Paetzold and Suprosanna Shit are supported by the Graduate School of Bioengineering, Technical University of Munich. We thank Mihail I. Todorov and Ali Ertrk.

References

1. Andres, B., et al.: Probabilistic image segmentation with closedness constraints. In: ICCV. pp. 2611–2618. IEEE (2011)
2. BenTaieb, A., Hamarneh, G.: Topology aware fully convolutional networks for histology gland segmentation. In: MICCAI. pp. 460–468. Springer (2016)
3. Çiçek, Ö., Aothers: 3D U-Net: learning dense volumetric segmentation from sparse annotation. In: MICCAI. pp. 424–432. Springer (2016)
4. Di Giovanna, A.P., et al.: Whole-brain vasculature reconstruction at the single capillary level. *Scientific reports* **8**(1), 12573 (2018)
5. Edelsbrunner, H., Harer, J.: Computational topology: an introduction. American Mathematical Soc. (2010)
6. Edelsbrunner, H., et al.: Topological persistence and simplification. In: FOCS. pp. 454–463. IEEE (2000)
7. Han, X., et al.: A topology preserving level set method for geometric deformable models. *IEEE TPAMI* **25**(6), 755–768 (2003)
8. Hu, K., et al.: Retinal vessel segmentation of color fundus images using multi-scale convolutional neural network with an improved cross-entropy loss function. *Neurocomputing* **309**, 179–191 (2018)
9. Hu, X., et al.: Topology-preserving deep image segmentation. In: NeurIPS. pp. 5658–5669 (2019)
10. Hunter, J.M., et al.: Morphological and pathological evolution of the brain microcirculation in aging and Alzheimers disease. *PloS one* **7**(5), e36893 (2012)
11. Joutel, A., et al.: Cerebrovascular dysfunction and microcirculation rarefaction precede white matter lesions in a mouse genetic model of cerebral ischemic small vessel disease. *JCI* **120**(2), 433–445 (2010)
12. Kirbas, C., Quek, F.: A review of vessel extraction techniques and algorithms. *CSUR* **36**(2), 81–121 (2004)

13. Kong, T.Y.: On topology preservation in 2-D and 3-D thinning. International journal of pattern recognition and artificial intelligence **9**(05), 813–844 (1995)
14. Kong, T.Y., Rosenfeld, A.: Digital topology: Introduction and survey. Computer Vision, Graphics, and Image Processing **48**(3), 357–393 (1989)
15. Lee, T.C., et al.: Building skeleton models via 3-D medial surface axis thinning algorithms. CVGIP: Graphical Models and Image Processing **56**(6), 462–478 (1994)
16. Ma, C.M.: On topology preservation in 3D thinning. CVGIP: Image understanding **59**(3), 328–339 (1994)
17. Milletari, F., et al.: V-net: Fully convolutional neural networks for volumetric medical image segmentation. In: 3DV. pp. 565–571. IEEE (2016)
18. Mnih, V.: Machine Learning for Aerial Image Labeling. Ph.D. thesis, University of Toronto (2013)
19. Mosinska, A., et al.: Beyond the pixel-wise loss for topology-aware delineation. In: CVPR. pp. 3136–3145 (2018)
20. Navarro, F., et al.: Shape-aware complementary-task learning for multi-organ segmentation. In: International Workshop on MLMI. pp. 620–627. Springer (2019)
21. Nowozin, S., Lampert, C.H.: Global connectivity potentials for random field models. In: CVPR. pp. 818–825. IEEE (2009)
22. Oswald, M.R., et al.: Generalized connectivity constraints for spatio-temporal 3D reconstruction. In: ECCV. pp. 32–46. Springer (2014)
23. Palágyi, K.: A 3-subiteration 3D thinning algorithm for extracting medial surfaces. Pattern Recognition Letters **23**(6), 663–675 (2002)
24. Phellan, R., et al.: Vascular segmentation in TOF MRA images of the brain using a deep convolutional neural network. In: MICCAI Workshop, pp. 39–46. Springer (2017)
25. Rempfler, M., et al.: Efficient algorithms for moral lineage tracing. In: ICCV. pp. 4695–4704 (2017)
26. Ronneberger, O., et al.: U-net: Convolutional networks for biomedical image segmentation. In: MICCAI. pp. 234–241. Springer (2015)
27. Schneider, M., et al.: Tissue metabolism driven arterial tree generation. Med Image Anal. **16**(7), 1397–1414 (2012)
28. Schneider, M., et al.: Joint 3-D vessel segmentation and centerline extraction using oblique Hough forests with steerable filters. Med Image Anal. **19**(1), 220–249 (2015)
29. Ségonne, F.: Active contours under topology controlgenus preserving level sets. International Journal of Computer Vision **79**(2), 107–117 (2008)
30. Shih, F.Y., Pu, C.C.: A skeletonization algorithm by maxima tracking on euclidean distance transform. Pattern Recognition **28**(3), 331–341 (1995)
31. Stuhmer, J., et al.: Tree shape priors with connectivity constraints using convex relaxation on general graphs. In: ICCV. pp. 2336–2343 (2013)
32. Sudre, C.H., et al.: Generalised dice overlap as a deep learning loss function for highly unbalanced segmentations. In: MICCAI Workshop, pp. 240–248. Springer (2017)
33. Taha, A.A., Hanbury, A.: Metrics for evaluating 3D medical image segmentation: analysis, selection, and tool. BMC Medical Imaging **15**(1), 29 (2015)
34. Tetteh, G., et al.: Deepvesselnet: Vessel segmentation, centerline prediction, and bifurcation detection in 3-d angiographic volumes. arXiv preprint arXiv:1803.09340 (2018)
35. Todorov, M.I., et al.: Machine learning analysis of whole mouse brain vasculature. Nature Methods pp. 1–8 (2020)
36. Türetken, E., et al.: Reconstructing curvilinear networks using path classifiers and integer programming. IEEE TPAMI **38**(12), 2515–2530 (2016)

37. Uslu, F., Bharath, A.A.: A multi-task network to detect junctions in retinal vasculature. In: MICCAI. pp. 92–100. Springer (2018)
38. Vicente, S., et al.: Graph cut based image segmentation with connectivity priors. In: CVPR. pp. 1–8. IEEE (2008)
39. Wegner, J.D., et al.: A higher-order CRF model for road network extraction. In: CVPR. pp. 1698–1705. IEEE (2013)
40. Wright, M.W., et al.: Skeletonization using an extended euclidean distance transform. *Image and Vision Computing* **13**(5), 367–375 (1995)
41. Zeng, Y., et al.: Topology cuts: A novel min-cut/max-flow algorithm for topology preserving segmentation in n-d images. *CVIU* **112**(1), 81–90 (2008)
42. Zhao, S., et al.: Cellular and molecular probing of intact human organs. *Cell* (2020)

A Additional qualitative results

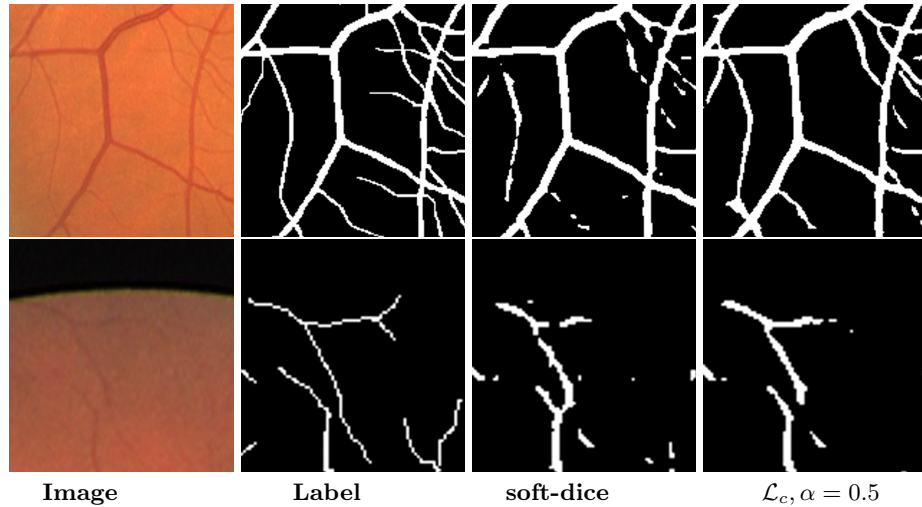


Fig. 9. Qualitative results: for the DRIVE retina dataset. From left to right, the real image, the label, the prediction using soft-dice and the U-Net predictions using $\mathcal{L}_c(\alpha = 0.5)$, respectively. This indicates that *soft-clDice* recovers retina vessel connections which the soft-dice loss misses.

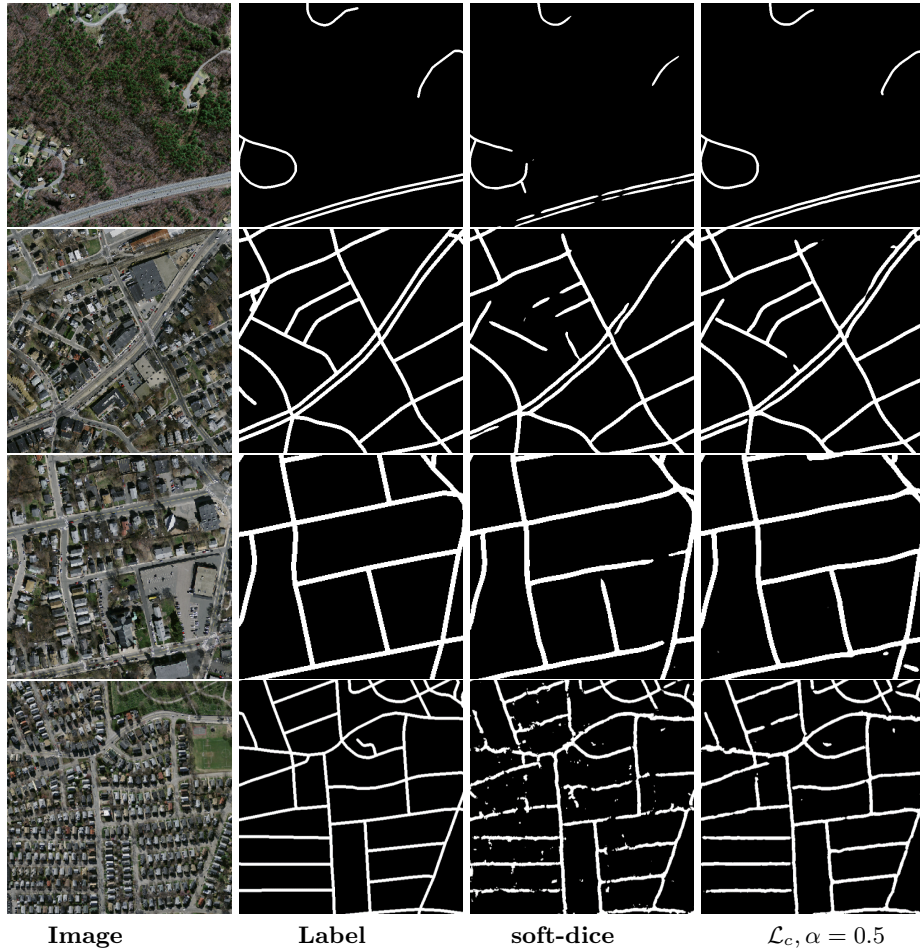


Fig. 10. Qualitative results: for the Massachusetts Road dataset. From left to right, the real image, the label, the prediction using soft-dice and the predictions using $\mathcal{L}_c(\alpha = 0.5)$, respectively. The first three rows are U-Net results and the last row is an FCN result. This indicates that *soft-clDice* segments road connections which the soft-dice loss misses.

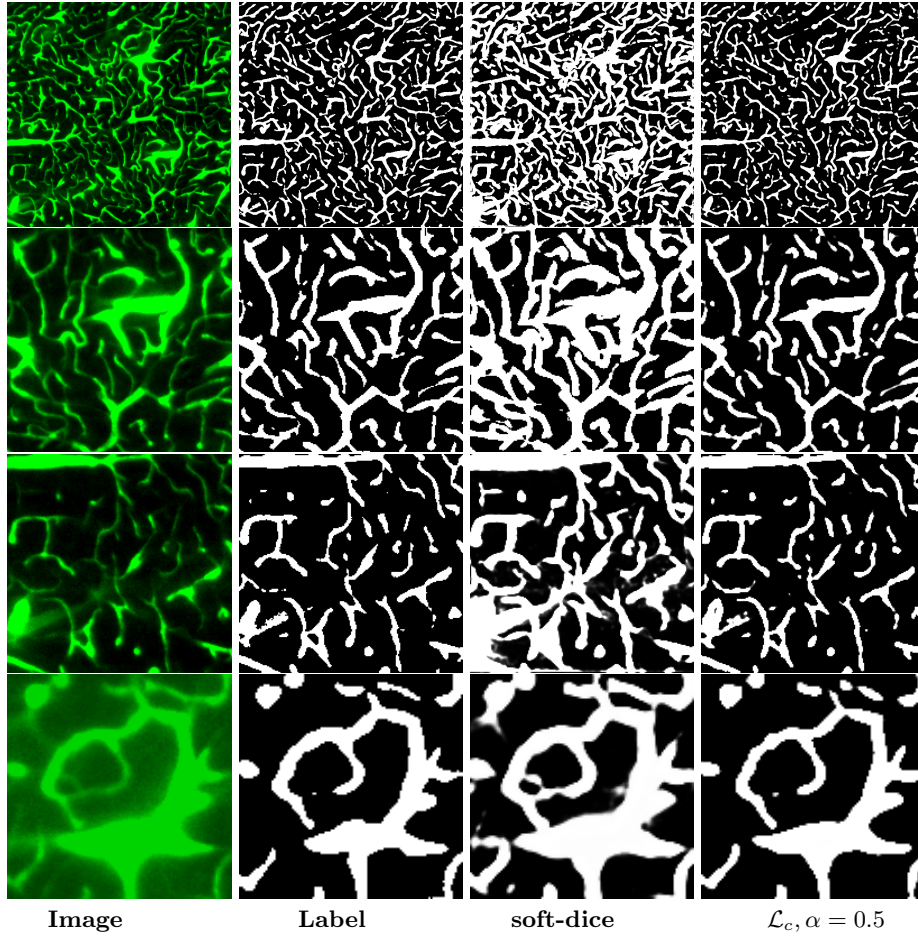


Fig. 11. Qualitative results: 2D slices of the 3D vessel dataset of different sized field of views. From left to right, the real image, the label, the prediction using soft-dice and the FCN predictions using $\mathcal{L}_c(\alpha = 0.5)$, respectively. These images show that *soft-clDice* helps to better segment the vessel connections. Importantly the networks trained using soft-dice over-segment the vessel radius and segments incorrect connections. Both of these errors are not present when we train including *soft-clDice* in the loss.

B Additional quantitative results

Table 4. Experimental results for 2D networks on the Massachusetts road dataset. Bold numbers indicate the best performance. All images are RGB (3 ch). Compared to *soft-Dice*, we observe that *soft-clDice* results in improved traditional scores for all $\alpha > 0$, *clDice* as well as an improved Euler characteristic χ_{ratio} agreement, for varying values of α .

Data	Network	Loss	Dice	clDice	Acc.	Dist.	Bifurc.	χ_{ratio}
Road-Network	FCN	<i>soft-dice</i>	64.84	70.79	95.16	0.88	0.56	28.22
		$\mathcal{L}_c, \alpha = 0.1$	66.52	74.80	95.70	0.86	0.65	15.41
		$\mathcal{L}_c, \alpha = 0.2$	67.42	76.25	95.80	0.86	0.67	13.73
		$\mathcal{L}_c, \alpha = 0.3$	65.90	74.86	95.35	0.87	0.61	15.39
		$\mathcal{L}_c, \alpha = 0.4$	67.18	76.92	95.46	0.91	0.67	15.35
		$\mathcal{L}_c, \alpha = 0.5$	65.77	75.22	95.09	0.91	0.71	17.39

C Network architectures

We use the following notation: In (input channels), Out (output channels), B (output channels) present input, output, and bottleneck information(for U-Net); C (filter size, output channels) denote a convolutional layer followed by *ReLU* and batch-normalization; U (filter size, output channels) denote a transposed convolutional layer followed by *ReLU* and batch-normalization; $\downarrow 2$ denotes maxpooling; \oplus indicates concatenation of information from an encoder block. We had to choose a different FCN architecture for the Massachusetts road dataset because we realize that a larger model is needed to learn useful features for this complex task.

C.1 Drive Dataset

FCN : $IN(3) \rightarrow C(3, 5) \rightarrow C(5, 10) \rightarrow C(5, 20) \rightarrow C(3, 50) \rightarrow C(1, 1) \rightarrow Out(1)$

Unet :

$ConvBlock : C_B(3, out\ size) \equiv C(3, out\ size) \rightarrow C(3, out\ size) \rightarrow \downarrow 2$

$UpConvBlock : U_B(3, out\ size) \equiv U(3, out\ size) \rightarrow \oplus \rightarrow C(3, out\ size)$

$Encoder : IN(3) \rightarrow C_B(3, 64) \rightarrow C_B(3, 128) \rightarrow C_B(3, 256) \rightarrow C_B(3, 512) \rightarrow C_B(3, 1024) \rightarrow B(1024)$

$$\text{Decoder} : B(1024) \rightarrow U_B(3, 1024) \rightarrow U_B(3, 512) \rightarrow U_B(3, 256) \rightarrow U_B(3, 128) \rightarrow U_B(3, 64) \rightarrow \text{Out}(1)$$

C.2 Road Dataset

$$\text{FCN} : IN(3) \rightarrow C(3, 10) \rightarrow C(5, 20) \rightarrow C(7, 30) \rightarrow C(11, 30) \rightarrow C(7, 40) \rightarrow C(5, 50) \rightarrow C(3, 60) \rightarrow C(1, 1) \rightarrow \text{Out}(1)$$

Unet : Same as Drive Dataset.

C.3 3D Dataset

$$\text{3D FCN} : IN(1/2) \rightarrow C(3, 5) \rightarrow C(5, 10) \rightarrow C(5, 20) \rightarrow C(3, 50) \rightarrow C(1, 1) \rightarrow \text{Out}(1)$$

3D Unet :

$$\text{ConvBlock} : C_B(5, \text{out size}) \equiv C(5, \text{out size}) \rightarrow C(5, \text{out size}) \rightarrow \downarrow 2$$

$$\text{UpConvBlock} : U_B(5, \text{out size}) \equiv U(5, \text{out size}) \rightarrow \oplus \rightarrow C(5, \text{out size})$$

$$\text{Encoder} : IN(1/2) \rightarrow C_B(5, 32) \rightarrow C_B(5, 64) \rightarrow C_B(5, 128) \rightarrow C_B(5, 256) \rightarrow B(256)$$

$$\text{Decoder} : B(256) \rightarrow U_B(5, 256) \rightarrow U_B(5, 128) \rightarrow U_B(5, 64) \rightarrow U_B(5, 32) \rightarrow \text{Out}(1)$$

Table 5. Total number of parameters for each of the architectures used in our experiment.

	Dataset	Network	Number of parameters
Drive	FCN	15.52K	
	UNet	28.94M	
Road	FCN	279.67K	
	3D FCN 2ch	58.71K	
	Unet 2ch	178.45M	

D Code for the *clDice* similarity measure and the *soft-clDice* loss (PyTorch):

D.1 *clDice* measure

```
from skimage.morphology import skeletonize
import numpy as np
def cl_score(v, s):
    return np.sum(v*s)/np.sum(s)
def clDice(v_p, v_l):
    tprec = cl_score(v_p, skeletonize(v_l))
    tsens = cl_score(v_l, skeletonize(v_p))
    return 2*tprec*tsens/(tprec+tsens)
```

D.2 *soft-clDice* in 2D

```
import torch.nn.functional as F
def soft_erode(img):
    p1 = -F.max_pool2d(-img, (3,1), (1,1), (1,0))
    p2 = -F.max_pool2d(-img, (1,3), (1,1), (0,1))
    return torch.min(p1,p2)

def soft_dilate(img):
    return F.max_pool2d(img, (3,3), (1,1), (1,1))

def soft_open(img):
    return soft_dilate(soft_erode(img))

def soft_skel(img, iter):
    img1 = soft_open(img)
    skel = F.relu(img-img1)
    for j in range(iter):
        img = soft_erode(img)
        img1 = soft_open(img)
        delta = F.relu(img-img1)
        skel = skel + F.relu(delta-skel*delta)
    return skel

def soft_c1Dice(v_p, v_l, iter = 50, smooth=1):
    s_p = soft_skel(v_p, iter)
    s_l = soft_skel(v_l, iter)
    tprec = ((s_p*v_l).sum()+smooth)/(s_p.sum()+smooth)
    tsens = ((s_l*v_p).sum()+smooth)/(s_l.sum()+smooth)
    return 2*tprec*tsens/(tprec+tsens)
```